Surfaces and Interfaces 84 (2026) 108587

Contents lists available at ScienceDirect

Surfaces and Interfaces

journal homepage: www.sciencedirect.com/journal/surfaces-and-interfaces

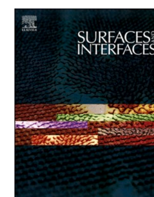

Isotropic thermal atomic layer etching of 2D MoS_2 using formic acid vapor

Hyewon Han [a,1], Jieun Kang [b,1], Jimin Kim [a], Sunjae Jeong [c], Siyeon Kim [c], Gahee Oh [c], Dahun Ko [c], Sihoon Son [d], Hyunbin Choi [a], Doosan Kim [b,e], Minjong Lee [f], Taesung Kim [g], Jiyoung Kim [e,f], Geunyoung Yeom [b,*]

[a] Department of Semiconductor Convergence Engineering, Sungkyunkwan University, 2066 Seobu-ro, Jangan-gu, Suwon-si, Gyeonggi-do 16419, South Korea
[b] Department of Advanced Materials Science & Engineering, Sungkyunkwan University, 2066 Seobu-ro, Jangan-gu, Suwon-si, Gyeonggi-do 16419, South Korea
[c] Department of Display Engineering, Sungkyunkwan University, 2066 Seobu-ro, Jangan-gu, Suwon-si, Gyeonggi-do 16419, South Korea
[d] SKKU Advanced Institute of Nanotechnology (SAINT), 2066 Seobu-ro, Jangan-gu, Suwon-si, Gyeonggi-do 16419, South Korea
[e] Department of Materials Science and Engineering, The University of Texas at Dallas, Richardson, TX 75080, USA
[f] Department of Electrical and Computer Engineering, The University of Texas at Dallas, Richardson, TX 75080, USA
[g] Departmemt of Mechanical Engineering, 2066 Seobu-ro, Jangan-gu, Suwon-si, Gyeonggi-do 16419, South Korea

ARTICLE INFO

Keywords:
MoS_2
Atomic layer etching
Isotropic etching
Remote oxygen plasma
Formic acid

ABSTRACT

Two-dimensional (2D) transition metal dichalcogenides (TMDs) such as 2D MoS_2 exhibit diverse electronic and optoelectronic properties depending on their thickness, making reliable layer control essential for their integration into advanced materials and devices. As device architecture evolves into three-dimensional configurations, highly layer controlled isotropic etching has become increasingly important. In this study, we introduce an isotropic thermal atomic layer etching (ALE) process of 2D MoS_2 monolayers for the fabrication of 3D devices through the surface modification of monolayer MoS_2 by a remote oxygen plasma, followed by exposure to formic acid vapor for the removal of the oxidized monolayer by a chemical reaction under annealing conditions. This approach enables highly controllable, layer-by-layer etching while minimizing surface damage, as confirmed by X-ray photoelectron spectroscopy (XPS), Raman spectroscopy, atomic force microscopy (AFM), and device-level measurements. Additionally, transmission electron microscopy (TEM) analysis of MoS_2 films suspended over three-dimensional trench structures confirmed the isotropic etching behavior. This study highlights the potential of organic-vapor-assisted ALE as a key technique for damage-free control of 2D material layer thickness, offering a promising pathway for next-generation semiconductor applications.

1. Introduction

Two-dimensional (2D) materials have garnered significant interest for next-generation electronics and optoelectronics owing to their tunable properties and atomically thin geometry [1–5]. Among them, molybdenum disulfide (MoS_2) is a representative transition metal dichalcogenide (TMD) with a thickness-dependent bandgap, transitioning from ~1.29 eV (indirect) in bulk to ~1.9 eV (direct) in the monolayer [6–8].

The unique electronic characteristics of MoS_2 not only make it a strong candidate for replacing silicon in planar devices but also underscore its potential in emerging three-dimensional (3D) device architectures such as gate-all-around (GAA) and complementary FET (CFET) configurations [9–11]. As device scaling approaches the sub-5 nm regime, silicon channels in CFETs suffer from severe mobility degradation. In contrast, 2D materials like MoS_2 can retain high mobility and low leakage current even at monolayer thickness, enabling high-performance operation of monolayer MoS_2 transistors even in the subthreshold regime [12,13]. Furthermore, its wide bandgap and high effective mass further suppress direct source-to-drain tunneling, offering clear advantages for sub-10 nm—and even sub-1 nm—gate lengths in three dimensional stacked GAA nanoribbon and CFET devices [14,15]. To fully realize these benefits in these devices, highly controlled and damage-free thickness control is essential, emphasizing the importance of isotropic atomic layer etching (ALE).

To achieve atomic-level thickness control of MoS_2, a variety of ALE strategies have been investigated. (Table 1) For example, chlorine radical adsorption followed by low-energy Ar^+ ion desorption enables

* Corresponding author.
E-mail address: gyyeom@skku.edu (G. Yeom).
[1] These authors contributed equally.

https://doi.org/10.1016/j.surfin.2026.108587
Received 15 December 2025; Received in revised form 21 January 2026; Accepted 23 January 2026
Available online 24 January 2026
2468-0230/© 2026 Elsevier B.V. All rights are reserved, including those for text and data mining, AI training, and similar technologies.

Table 1
Comparison of previously reported MoS_2 ALE processes and this work.

Reference #	Gas	Direction	Temperature
15	Cl, Ar	Anisotropy	RT
16	O_2	Isotropy	500 °C
17	MoF_6, H_2O	Isotropy	150–300 °C (500 °C for the removal of residual MoO_x)
This work	O_2, Formic acid	Isotropy	300 °C

anisotropic, atomic layer etching with minimal substrate damage; however, its anisotropic nature makes it difficult to apply to three-dimensional structures [16]. Remote O_2 plasma oxidation followed by high-temperature annealing (≥500 °C) can remove oxidized layers but the high thermal budget limits compatibility with device integration [17]. Thermal ALE using MoF_6 and H_2O achieves isotropic etching at 150–300 °C, yet leaves residual MoO_x requiring additional 500 °C desorption for surface cleaning [18].

Therefore, we propose a formic acid-assisted ALE process for MoS_2 that enables isotropic, layer-by-layer removal at low temperatures (~300 °C) while avoiding the drawbacks of prior methods. The process alternates (i) surface modification of a MoS_2 monolayer by oxygen radicals from a remote plasma and (ii) thermally driven desorption of the modified layer by chemical reaction via formic acid vapor exposure. This method enables reliable thickness control without apparent damage even under repeated cyclic process, and its successful application to chemical vapor deposition (CVD)-grown MoS_2 films demonstrates strong potential for wafer-scale fabrication. Accordingly, this isotropic thermal ALE provides a promising pathway for the integration of 2D materials into advanced 3D device architectures.

2. Experimental

2.1. Sample preparation

Monolayer and multilayer (over 5 layers) CVD-grown MoS_2 films (1 cm x 1 cm) were purchased from 6Carbon Co., Ltd. and monolayer MoS_2 films were transferred onto SiO_2/Si substrates to prepare the bilayer and trilayer MoS_2 samples. For transfer, polymethyl methacrylate (PMMA; 495 PMMA A6, Kayaku Advanced Materials) was spin-coated onto the as-grown monolayer MoS_2, and thermal release tape (TRT) was attached. The TRT-supported film was separated in deionized water (18.2 MΩ·cm, ELGA LabWater), and subsequent stacking steps were performed without PMMA coating. The resulting stacks were aligned on SiO_2/Si substrates and released by heating at 110 °C. Residual PMMA was removed by sequential rinsing with acetone and isopropyl alcohol (IPA; 2-propanol, 99.9 %, Samchun). For isotropy experiments, MoS_2 was transferred onto oxide trench-patterned substrates with a 30 nm spacing, resulting in suspended regions suitable for cross-sectional analysis.

2.2. Thermal atomic layer etching of MoS_2

MoS_2 samples were exposed to oxygen radicals generated in a remote inductively coupled plasma (ICP) reactor equipped with dual crossed-hole grids, which effectively blocked energetic ions from reaching the substrate. The plasma was ignited under an O_2 pressure of 100 mTorr with a 13.56 MHz radio-frequency (RF) power of 300 W at 200 °C. Subsequent removal of the oxidized surface layer was carried out by exposing it to formic acid (FA) vapor mixed with nitrogen (FA:N_2 = 1:2) at 300 °C. The substrate temperature was monitored using a thermocouple in direct contact with the sample holder and further validated by a surface temperature-indicating label (THERMAX, 5-grid thermometer).

2.3. Device fabrication

Bottom-gated FETs were fabricated using CVD-grown MoS_2 transferred onto Si substrates with a 300 nm SiO_2 dielectric and heavily doped p-type Si (p^{++}) (TASCO) serving as the global back-gate electrode. Following transfer, source and drain electrodes were defined by photolithography. Chromium (5 nm) and gold (50 nm) were subsequently deposited via electron-beam evaporation to form the contacts. The lift-off process was carried out in acetone, and the samples were then rinsed sequentially with isopropyl alcohol and deionized water to

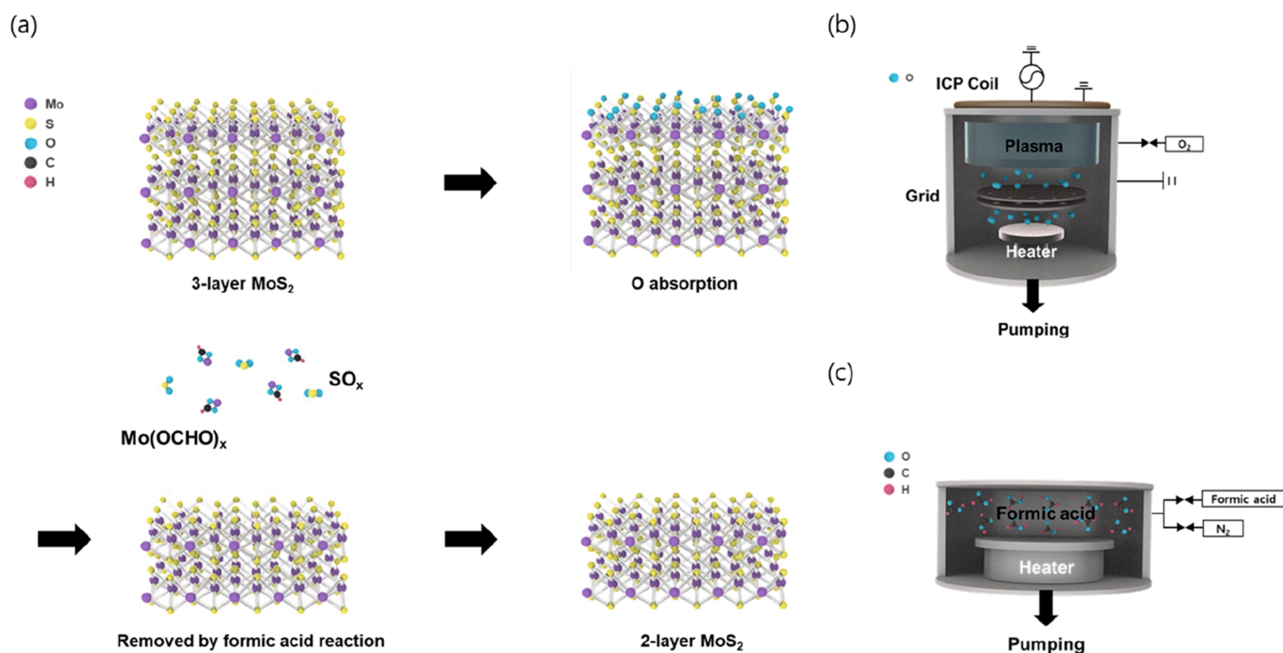

Fig. 1. Schematic illustration of (a) an ALE cycle for MoS_2 consisting of oxidation and formic acid reaction steps, (b) a remote inductively coupled plasma (ICP) system with dual grids for oxidation, and (c) a formic acid treatment system for desorption by reaction.

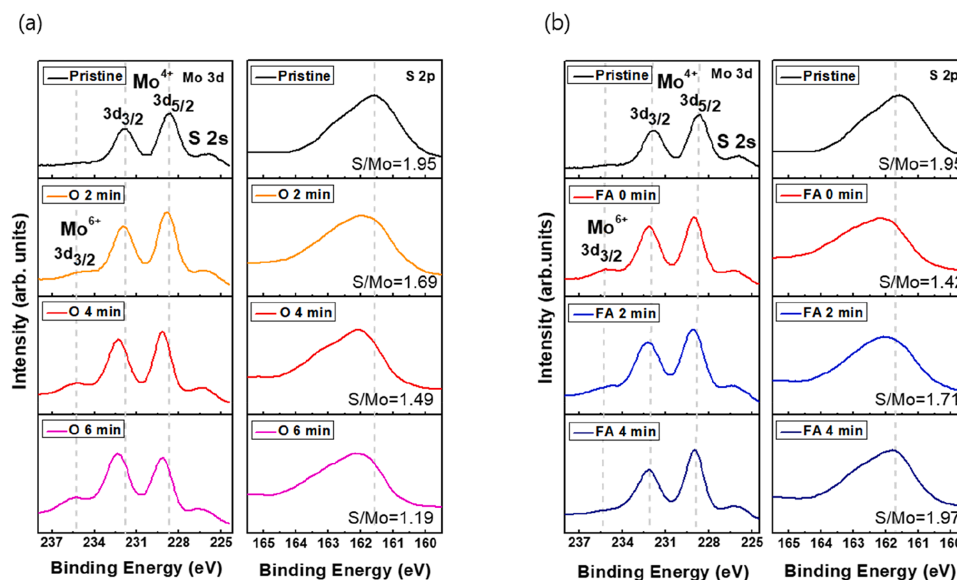

Fig. 2. X-ray photoelectron spectroscopy (XPS) spectra of Mo 3d and S 2p on a bilayer MoS_2 surface according to the (a) oxygen radical exposure time (pristine, 2, 4, and 6 min) and (b) formic acid vapor exposure time (pristine, 0, 2, and 4 min) following 4 min of oxidation.

remove residual resist and solvents.

2.4. Characterization methods

2.4.1. Raman and photoluminescence spectroscopy

Raman and photoluminescence (PL) spectra were measured using a confocal Raman microscope (WITec Alpha 300 *M*+) with a 532 nm excitation laser. These measurements were used to evaluate the layer number and bandgap characteristics of the MoS_2 before and after ALE processing.

2.4.2. X-ray photoelectron spectroscopy

XPS (XPS, MultiLab 2000, Thermo VG, Mg Kα source) was employed to analyze the chemical composition and oxidation states. A monochromatic Al Kα X-ray gun operated at 12 kV and 180 W was used with an Alpha110 hemispherical electron energy analyzer. High-resolution spectra were collected using a pass energy of 30 eV and a step size of 0.1 eV. A Shirley background was subtracted from all spectra, and the binding energies were calibrated to the C 1 s peak at 284.8 eV to correct for charging effects.

2.4.3. Atomic force microscopy

Surface morphology and thickness evolution were characterized using AFM (Park Systems, XE-100) operated in non-contact mode with a PPP-NCHR silicon cantilever (spring constant ≈ 42 N/m, resonance frequency ≈ 330 kHz). Both height profiles and root-mean-square (RMS) surface roughness were analyzed at each ALE step.

2.4.4. High-resolution scanning transmission electron microscopy

HR-TEM/STEM analysis was carried out using a JEOL JEM-ARM200F operated at an accelerating voltage of 200 kV with a ZrO/W(100) Schottky field-emission electron source. High-angle annular dark-field (HAADF) STEM imaging was employed to directly visualize the MoS_2 lattice and to determine the number of layers with atomic-scale contrast. The instrument provides a HAADF-STEM resolution of ~0.1 nm, enabling clear identification of layer stacking and structural evolution in suspended MoS_2 films across oxide trench patterns.

2.4.5. Electrical and optoelectronic measurements

Electrical properties of MoS_2 field-effect transistors were measured using a semiconductor parameter analyzer (Keithley 4200A-SCS) in a probe station. Threshold voltage and current level changes were monitored as a function of thickness in transfer curves. Photoresponse measurements were performed under pulsed illumination using red (650 nm) and blue (450 nm) light sources to probe optoelectronic performance.

3. Results and discussion

Fig. 1 presents the schematic illustration and experimental setup of the ALE process for MoS_2. As shown in Fig. 1a, the ALE cycle used in the experiment consists of two sequential steps: (i) oxidation of the MoS_2 surface by reactive oxygen radicals, followed by (ii) removal of the oxidized layer through a chelation-type reaction with a vaporized formic acid. This two-step sequence enables atomic-scale layer-by-layer thinning of MoS_2. The oxidation step was conducted in a remote inductively coupled plasma (ICP) system equipped with dual crossed-hole grids, shown in Fig. 1b The grid structure prevented energetic ions from reaching the substrate while permitting neutral radicals to interact with the surface, thereby ensuring chemical oxidation without plasma-induced physical damage. In addition, the SiC heater located beneath the sample holder supplied thermal energy to enhance surface reactivity, that is, by performing the oxidation at 200 °C to achieve efficient and controlled surface modification. Following the oxidation step, the sample was introduced into an organic vapor treatment, as shown in Fig. 1c. In this step, vaporized formic acid carried by a N_2 gas flow reacted with the surface oxide species via a chelation mechanism. The oxidized Mo *species* were bonded with the carboxyl group in the formic acid to form volatile compound layer, which were subsequently desorbed from the surface [19]. The substrate was heated to 300 °C to supply sufficient thermal energy for desorption of the compound layer. Repetition of the oxidation and desorption sequence defines the cyclic isotropic thermal ALE cycle, providing layer-by-layer thickness control without introducing noticeable damage to the underlying lattice.

To investigate the ALE characteristics of MoS_2, involving an oxidation step followed by removal through formic acid vapor treatment, X-ray photoelectron spectroscopy (XPS) analysis was performed. Fig. 2a and 2b present the XPS spectra of Mo 3d and S 2p on a bilayer CVD-grown MoS_2 surface as a function of oxygen radical exposure time and formic acid vapor exposure time, respectively. As shown in Fig. 2a, with increasing oxygen radical exposure, a Mo^{6+} peak —a clear signature of Mo—O bond formation—emerges in the Mo 3d region. Consistently, the

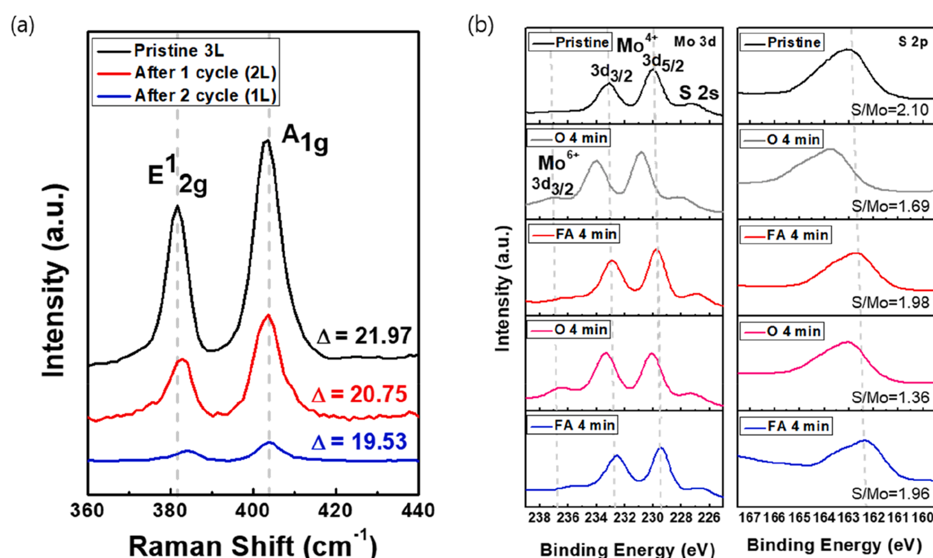

Fig. 3. (a) Raman spectra of a trilayer MoS_2 measured over two ALE cycles. (b) XPS spectra of a trilayer MoS_2 measured at each step over two ALE cycles consisting of sequential oxidation and formic acid vapor treatment.

S/Mo atomic ratio, calculated from Table S1, decreases from 1.95 (pristine) to 1.69, 1.49, and 1.19 with increasing oxidation time, confirming the progressive formation of surface oxide layer (MoS_xO_y) on MoS_2 [20]. The shift of Mo 3d and S 2p peaks toward higher binding energies arises from oxygen substitution-induced lattice distortions and vacancy defects, which introduce donor states in the band gap of MoS_2 and alter carrier transport [21–24]. Fig. 2b shows the XPS spectra after a 4 min oxidation step followed by sequential formic acid treatments. With increasing formic acid vapor exposure time, the Mo^{6+} peak introduced during oxidation is gradually suppressed and nearly disappears after 4 min, indicating complete removal of the oxidized layer. Simultaneously, the binding energy positions return toward those of the pristine sample, and the S/Mo ratio recovers to 1.71 and 1.97 after 2 and 4 min of formic acid treatment, respectively. After 4 min of formic acid vapor exposure, both the peak positions and stoichiometry are nearly restored to the pristine state. This recovery indicates that the structural and compositional changes induced by oxygen substitution during oxidation are reversed as the oxidized surface layer is selectively removed by the formic acid reaction. Moreover, formic acid treatment alone did not produce noticeable changes, and oxidation followed by annealing without formic acid also showed no significant alteration. (Figure S2) These observations confirm the proposed ALE mechanism, in which oxygen radical exposure oxidizes the surface layer and subsequent formic acid vapor treatment selectively removes the resulting

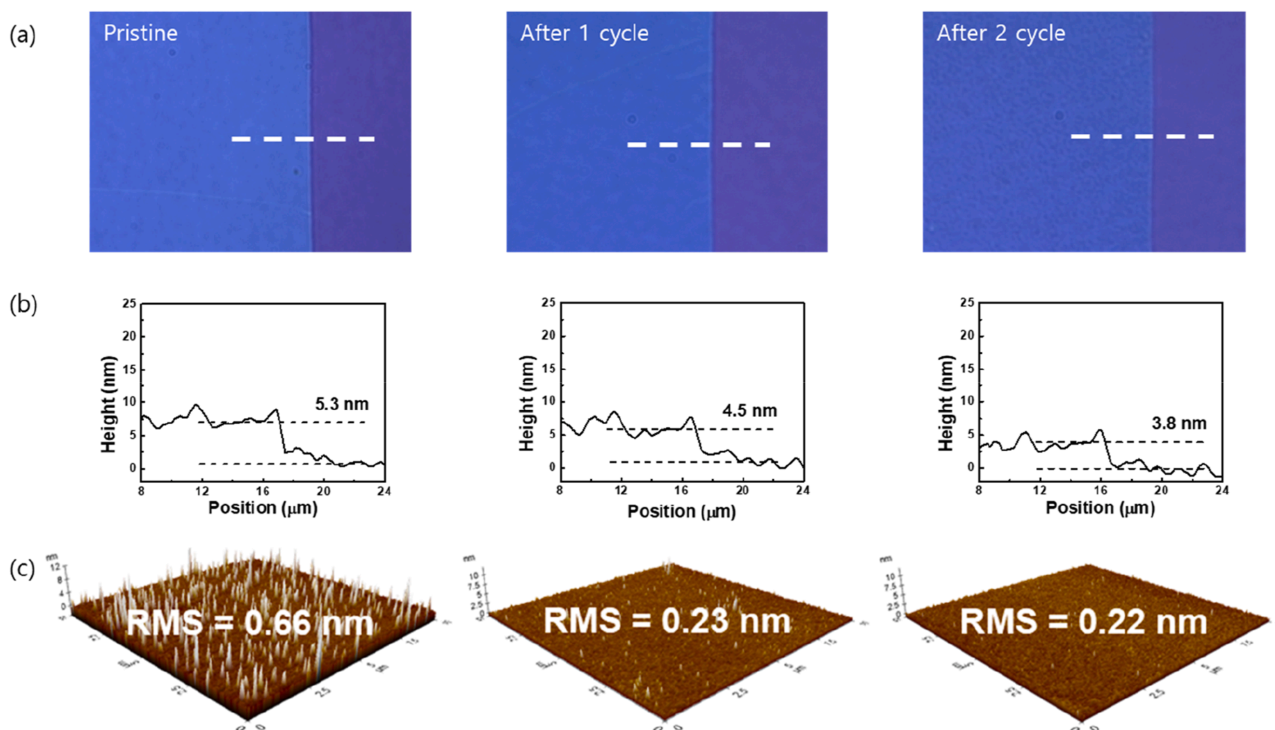

Fig. 4. (a) Optical images, (b) atomic force microscopy (AFM) height profile, and (c) root mean square (RMS) surface roughness images of a multilayer MoS_2 measured at each step over two ALE cycles consisting of sequential oxidation and formic acid vapor treatment.

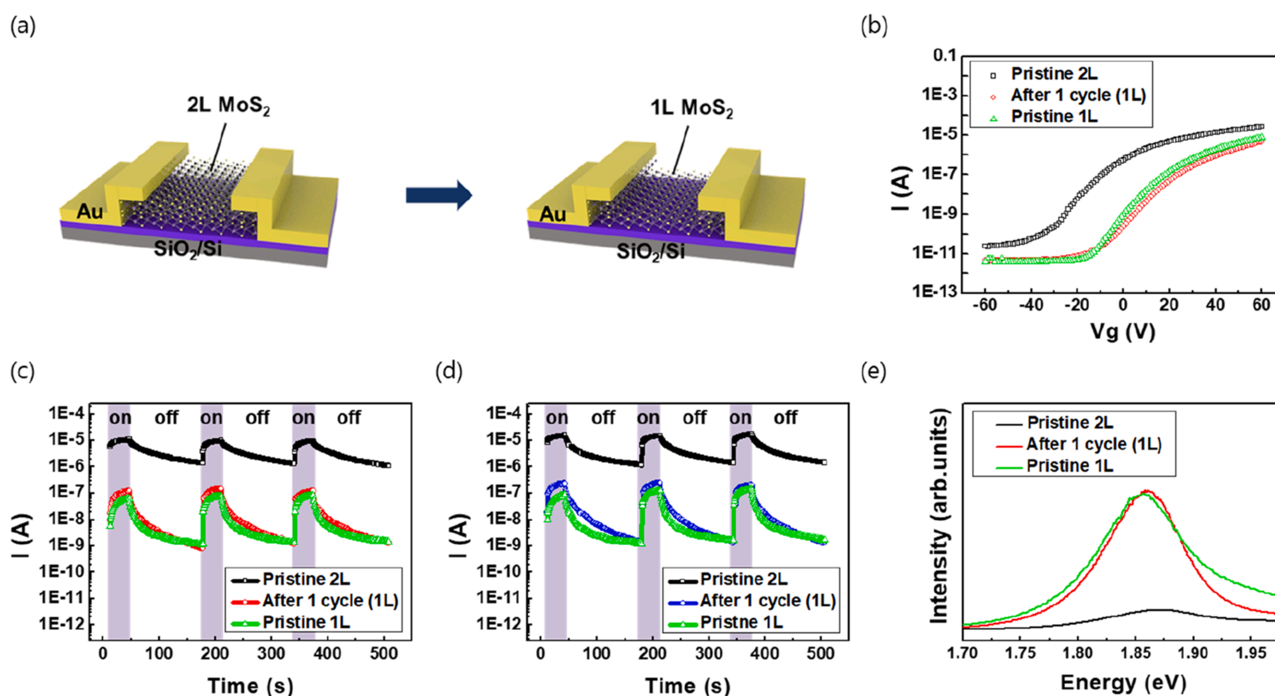

Fig. 5. (a) Schematic illustration of bilayer MoS_2 bottom-gate field-effect transistors (FETs) before and after one ALE cycle. (b) Transfer curves, photocurrent responses under pulsed (c) red- and (d) blue-light illumination, and (e) photoluminescence (PL) spectra for pristine bilayer, after one ALE cycle, and pristine monolayer MoS_2 FETs.

oxide, enabling layer-by-layer thinning of MoS_2.

The cyclic nature of the proposed ALE process was further verified using Raman spectroscopy and XPS, as shown in Fig. 3. Fig. 3a shows the Raman spectra of trilayer MoS_2 after successive ALE cycles. For the pristine trilayer, the separation (Δ) between the E^1_{2g} and A_{1g} modes was 21.97 cm^{-1}. After the first and second ALE cycles, this separation decreased to 20.75 cm^{-1} and 19.53 cm^{-1}, respectively, values consistent with previously reported layer-dependent Raman shifts for bilayer and monolayer MoS_2 [16,25–27]. These results demonstrate that one atomic layer is removed in each ALE cycle. Fig. 3b presents the XPS spectra measured at each step of two ALE cycles. After oxidation step, the Mo^{6+} component appeared along with a binding energy shift, while subsequent formic acid treatment removed the oxidized layer and restored both the peak positions and the S/Mo ratio to near-pristine values, consistent with Fig. 2. Importantly, this behavior was reproduced in the second ALE cycle as well, confirming that the process can be repeated without introducing cumulative structural damage or compositional degradation.

To further analyze thickness evolution, atomic force microscopy (AFM) measurements were performed. For accurate thickness determination, a multilayer CVD-grown MoS_2 was transferred onto a 300-nm SiO_2/Si substrate, and the step height between the film and substrate was measured. The optical images of the transferred samples at each ALE step are shown in Fig. 4a. As presented in Fig. 4b, the thickness of the pristine multilayer MoS_2 was 5.3 nm, which decreased to 4.5 nm after the first ALE cycle and to 3.8 nm after the second cycle. This corresponds to an etch rate of ~0.7–0.8 nm per cycle, consistent with the theoretical thickness of a monolayer MoS_2 layer, confirming once again the layer-by-layer nature of the process. In parallel, the root mean square (RMS) surface roughness was evaluated across a 1 × 1 cm^2 sample by dividing it into nine measurement points (Figure S3). The central region, shown in Fig. 4c, revealed that pristine CVD MoS_2 exhibited an RMS roughness of 0.66 nm, which decreased markedly to 0.23 nm after the first ALE cycle. This reduction can be attributed to the removal of protruding MoS_x domains formed during the CVD growth [28,29]: oxygen radicals preferentially adsorb on these extruded regions, and subsequent formic acid vapor treatment removes them, thereby reducing local surface irregularities. As a result, the isotropic reactions of radicals and vapor promote uniform smoothing across the surface [19]. After the second ALE cycle, the RMS roughness remained low at 0.22 nm, indicating that repeated cycles maintain a smooth surface without introducing additional surface damage. The reduced and stabilized roughness demonstrates that the ALE process uniformly smooths the MoS_2 surface over a large area.

The electrical and optoelectronic properties of MoS_2 after one ALE cycle were further investigated using bilayer bottom-gate field-effect transistors (FETs) shown in Fig. 5a. As shown in Fig. 5b, the transfer characteristic of the device after one ALE cycle is nearly identical to that of pristine monolayer MoS_2. From these transfer curves, the field-effect mobility was extracted as 12.03 $cm^2 V^{-1} s^{-1}$ for pristine 2 L, 2.07 $cm^2 V^{-1} s^{-1}$ for the etched monolayer (after 1 cycle), and 3.41 $cm^2 V^{-1} s^{-1}$ for pristine 1 L devices, indicating that the etched monolayer exhibits a mobility comparable in order to the pristine monolayer. These results demonstrate that the thinning process preserves device functionality. Also, the transfer characteristics of the MoS_2 FET after one ALE cycle were re-measured after 7 days and the results showed the similar characteristics exhibiting good stability (Figure S5). Fig. 5c and 5d display the photocurrent responses under pulsed red- and blue-light excitation, respectively. The device subjected to one cycle of etching exhibits an enhanced photocurrent on/off ratio, approaching the values of pristine monolayer MoS_2. This enhanced photocurrent on/off ratio can be attributed to the direct band gap nature of monolayer MoS_2, which enables stronger optical absorption and more efficient electron-hole pair generation under illumination, in contrast to the indirect band gap bilayer that exhibits distinct optoelectronic characteristics [30,31]. Complementary evidence is provided by the photoluminescence (PL) spectra shown in Fig. 5e. After one ALE cycle, the PL intensity increases markedly compared to pristine bilayer MoS_2 and closely resembles that of pristine monolayer MoS_2. This observation confirms that the etched sample has transitioned to a monolayer with a direct band gap. Collectively, these results demonstrate that the proposed ALE method enables reliable layer control of MoS_2 while preserving

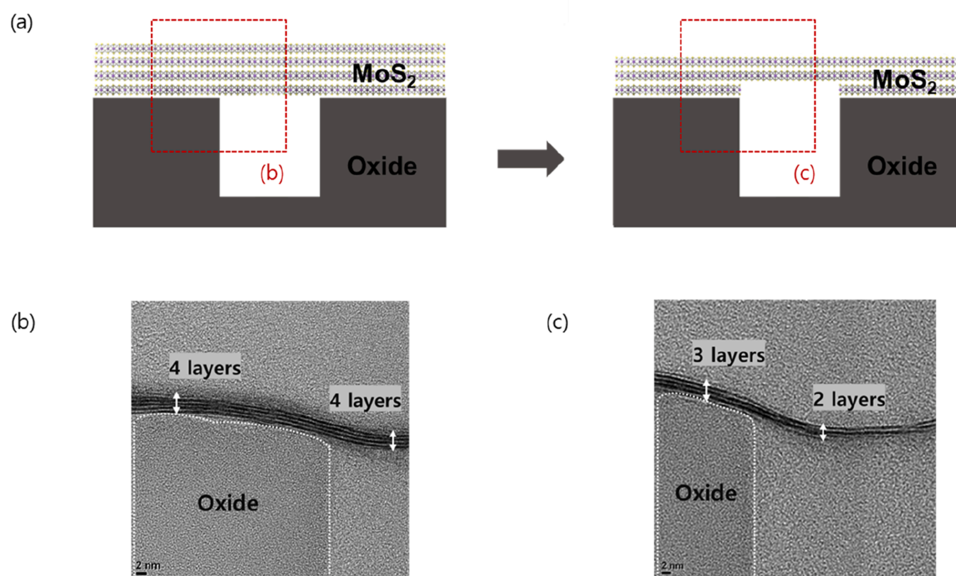

Fig. 6. (a) Schematic illustration of a four-layer MoS_2 transferred onto an oxide trench-patterned substrate before and after one ALE cycle. Cross-sectional TEM images of the trench region showing the layered structure of MoS_2 (b) before and (c) after one ALE cycle.

high-quality electrical and optical performance at the device level.

Fig. 6a illustrates the process schematic designed to probe the isotropic nature of the proposed ALE method. A four-layer MoS_2 film was transferred onto an oxide trench pattern with a 30 nm spacing, creating a suspended three-dimensional configuration [32]. The presence of this suspended structure was further confirmed by energy-dispersive X-ray spectroscopy (EDS) mapping, as shown in Figure S4. Following one ALE cycle, the structural evolution was examined by cross-sectional TEM. As shown in Fig. 6b, the reference TEM image confirms that both the supported and suspended regions of the transferred MoS_2 film maintained a uniform thickness of four layers prior to etching. In contrast, after one ALE cycle (Fig. 6c), the supported region on the oxide trench was reduced to three layers, while the suspended region decreased by two layers, yielding a bilayer structure. This difference arises from the non-directional nature of both the oxygen radicals and formic acid vapor, which can penetrate through the trench void and access the MoS_2 surface from all directions. Consequently, regions exposed from both the top and bottom were etched within one ALE cycle. These results clearly demonstrate the isotropic characteristics of the ALE process and validate its suitability for application to three-dimensional device architectures.

4. Conclusions

In this work, we demonstrated an isotropic thermal ALE process for MoS_2 using a remote oxygen plasma and a formic acid vapor, operating at a relatively low temperature (~300 °C) compared with previous thermal ALE approaches for MoS_2. The process proceeds via surface oxidation of the topmost MoS_2 layer followed by its removal through a chelation reaction with formic acid, thereby enabling controlled, cycle-by-cycle thinning of monolayers while minimizing structural damage. These characteristics were systematically confirmed through spectroscopic, microscopic, and device-level characterizations. XPS and Raman analyses verified the sequential oxidation-desorption mechanism and confirmed layer-by-layer thickness control, while AFM measurements revealed smooth surface morphology preserved after multiple etch cycles. Electrical and optoelectronic measurements of bilayer field-effect transistors further showed that devices subjected to one cycle ALE exhibited characteristics consistent with monolayer MoS_2, underscoring the preservation of material quality and functionality. Moreover, cross-sectional TEM analysis of suspended MoS_2 films over oxide trench structures directly demonstrated the isotropic nature of the process, highlighting its applicability to three-dimensional device architectures. Overall, these results establish organic-vapor-assisted ALE as a versatile and damage-free strategy for controlled thinning of two-dimensional semiconductors. The combination of isotropic etching behavior, large-area uniformity, and integration compatibility highlights its potential as an enabling platform for incorporating 2D materials into next-generation 3D semiconductor technologies.

Data availability

Data will be made available on request.

CRediT authorship contribution statement

Hyewon Han: Writing – original draft, Validation, Methodology, Investigation, Formal analysis, Conceptualization. **Jieun Kang:** Methodology, Investigation, Formal analysis, Conceptualization, Writing – original draft. **Jimin Kim:** Formal analysis, Data curation, Conceptualization, Writing – original draft. **Sunjae Jeong:** Formal analysis, Validation, Writing – review & editing. **Siyeon Kim:** Data curation, Writing – review & editing. **Gahee Oh:** Investigation, Resources, Writing – review & editing. **Dahun Ko:** Resources, Investigation, Writing – review & editing. **Sihoon Son:** Data curation, Writing – review & editing. **Hyunbin Choi:** Writing – review & editing, Formal analysis. **Doosan Kim:** Writing – review & editing, Validation. **Minjong Lee:** Writing – review & editing, Validation. **Taesung Kim:** Supervision, Conceptualization, Writing – review & editing. **Jiyoung Kim:** Supervision, Conceptualization, Writing – review & editing. **Geunyoung Yeom:** Writing – review & editing, Supervision, Project administration, Data curation, Conceptualization.

Declaration of competing interest

The authors declare that they have no known competing financial interests or personal relationships that could have appeared to influence the work reported in this paper.

Acknowledgments

This work was supported by the Technology Innovation Program

(Public-private joint investment semiconductor R&D program (K-CHIPS) to foster high-quality human resources) (RS-2023-00235484, “Development of High Quality MX2 Materials and Processes through In situ Defect Analy-sis”) funded by the Ministry of Trade, Industry & Energy (MOTIE, Korea) (1415187770) and a National Research Foundation of Korea (NRF) grant funded by the Korea government (MSIT) (No. 2022R1A2C2091660).

Supplementary materials

Supplementary material associated with this article can be found, in the online version, at doi:10.1016/j.surfin.2026.108587.

References

[1] W. Choi, M.Y. Cho, A. Konar, J.H. Lee, G.B. Cha, S.C. Hong, S. Kim, J. Kim, D. Jena, J. Joo, S. Kim, High-detectivity multilayer MoS_2 phototransistors with spectral response from ultraviolet to infrared, Adv. Mater. 24 (2012) 5832–5836, https://doi.org/10.1002/adma.201201909.

[2] Q.H. Wang, K. Kalantar-Zadeh, A. Kis, J.N. Coleman, M.S. Strano, Electronics and optoelectronics of two-dimensional transition metal dichalcogenides, Nat. Nanotechnol. 7 (2012) 699–712, https://doi.org/10.1038/nnano.2012.193.

[3] T. Cao, G. Wang, W. Han, H. Ye, C. Zhu, J. Shi, Q. Niu, P. Tan, E. Wang, B. Liu, J. Feng, Valley-selective circular dichroism of monolayer molybdenum disulphide, Nat. Commun. 3 (2012) 887, https://doi.org/10.1038/ncomms1882.

[4] Y.H. Lee, X.Q. Zhang, W. Zhang, M.T. Chang, C.T. Lin, K.D. Chang, Y.C. Yu, J.T. W. Wang, C.S. Chang, L.J. Li, T.W. Lin, Synthesis of large-area MoS_2 atomic layers with chemical vapor deposition, Adv. Mater. 24 (2012) 2320–2325, https://doi.org/10.1002/adma.201104798.

[5] D. Dumcenco, D. Ovchinnikov, K. Marinov, P. Lazic, M. Gibertini, N. Marzari, O. L. Sanchez, Y.C. Kung, D. Krasnozhon, M. Chen, S. Bertolazzi, P. Gillet, A. Fontcuberta i Morral, A. Radenovic, A. Kis, Large-area epitaxial monolayer MoS_2, ACS Nano 9 (2015) 4611–4620, https://doi.org/10.1021/acsnano.5b01281.

[6] O. Lopez-Sanchez, D. Lembke, M. Kayci, A. Radenovic, A. Kis, Ultrasensitive photodetectors based on monolayer MoS_2, Nat. Nanotechnol. 8 (2013) 497–501, https://doi.org/10.1038/nnano.2013.100.

[7] B. Radisavljevic, A. Radenovic, J. Brivio, V. Giacometti, A. Kis, Single-layer MoS_2 transistors, Nat. Nanotechnol. 6 (2011) 147–150, https://doi.org/10.1038/nnano.2010.279.

[8] K.F. Mak, C. Lee, J. Hone, J. Shan, T.F. Heinz, Atomically thin MoS_2: a new direct-gap semiconductor, Phys. Rev. Lett. 105 (2010) 136805, https://doi.org/10.1103/PhysRevLett.105.136805.

[9] S.B. Desai, S.R. Madhvapathy, A.B. Sachid, J.P. Llinas, Q. Wang, G.H. Ahn, G. Pitner, M.J. Kim, J. Bokor, C. Hu, H.S.P. Wong, A. Javey, MoS_2 transistors with 1-nanometer gate lengths, Science 354 (2016) 99–102, https://doi.org/10.1126/science.aah4698.

[10] H. Liu, A.T. Neal, P.D. Ye, Channel length scaling of MoS_2 MOSFETs, ACS Nano 6 (2012) 8563–8569, https://doi.org/10.1021/nn303513c.

[11] D. Sarkar, X. Xie, W. Liu, W. Cao, J. Kang, Y. Gong, S. Kraemer, P.M. Ajayan, K. Banerjee, A subthermionic tunnel field-effect transistor with an atomically thin channel, Nature 526 (2015) 91–95, https://doi.org/10.1038/nature15387.

[12] Y. Liu, X. Duan, H.J. Shin, S. Park, Y. Huang, X. Duan, Promises and prospects of two-dimensional transistors, Nature 591 (2021) 43–53, https://doi.org/10.1038/s41586-021-03339-z.

[13] M. Liu, J. Niu, G. Yang, R. Zhao, K. Chen, W. Lu, F. Liao, Z. Wu, C. Jiang, D. Geng, N. Lu, A. Nathan, L. Li, M. Liu, Subthreshold Schottky-barrier transistor based on monolayer molybdenum disulfide, Nat. Commun. (2025), https://doi.org/10.1038/s41467-025-67347-7.

[14] K.P. O'Brien, C.H. Naylor, C. Dorow, K. Maxey, A.V. Penumatcha, A. Vyatskikh, T. Zhong, A. Kitamura, S. Lee, C. Rogan, W. Mortelmans, M.S. Kavrik, R. Steinhardt, P. Buragohain, S. Dutta, T. Tronic, S. Clendenning, P. Fischer, E. S. Putna, M. Radosavljevic, M. Metz, U. Avci, Process integration and future outlook of 2D transistors, Nat. Commun. 14 (2023) 7684, https://doi.org/10.1038/s41467-023-41779-5.

[15] M. Liu, J. Niu, G. Yang, K. Chen, W. Lu, F. Liao, C. Lu, N. Lu, L. Li, Large-scale ultrathin channel nanosheet-stacked CFET based on CVD 1L MoS_2/WSe_2, Adv. Electron. Mater. 9 (2023) 2200849, https://doi.org/10.1002/aelm.202200722.

[16] K.S. Kim, K.H. Kim, Y. Nam, J. Jeon, S. Yim, E. Singh, J.Y. Lee, S.J. Lee, Y.S. Jung, G.Y. Yeom, D.W. Kim, Atomic layer etching mechanism of MoS_2 for nanodevices, ACS Appl. Mater. Interfaces 9 (2017) 11967–11976, https://doi.org/10.1021/acsami.6b15886.

[17] H. Zhu, X. Qin, L. Cheng, A. Azcatl, J. Kim, R.M. Wallace, Remote plasma oxidation and atomic layer etching of MoS_2, ACS Appl. Mater. Interfaces 8 (2016) 19119–19126, https://doi.org/10.1021/acsami.6b04719.

[18] J. Soares, A.U. Mane, D. Choudhury, S. Letourneau, S.M. Hues, J.W. Elam, E. Graugnard, Thermal atomic layer etching of MoS_2 using MoF_6 and H_2O, Chem. Mater. 35 (2023) 927–936, https://doi.org/10.1021/acs.chemmater.2c02549.

[19] J.E. Kang, Y. Choi, H.W. Han, J.M. Kim, Y.E. Kim, H. Seok, T. Kim, D.S. Kim, G. Y. Yeom, Cyclic atomic layer etching of $PdSe_2$, Adv. Funct. Mater. 34 (2024) 2408154, https://doi.org/10.1002/adfm.202408154.

[20] T.Y. Ko, A. Jeong, W. Kim, J. Lee, Y. Kim, J.E. Lee, G.H. Ryu, K. Park, D. Kim, Z. Lee, On-stack two-dimensional conversion of MoS_2 into MoO_3, 2D Mater 4 (2017) 014003, https://doi.org/10.1088/2053-1583/4/1/014003.

[21] J. Kim, J. Kang, H. Han, S. Jeong, S. Kim, H. Lee, H. Kim, Y. Kim, G. Yeom, From N-type doping to phase transition in large-area MoS_2 via controlled sulfur vacancy formation, Nanoscale 17 (2025) 24773–24781, https://doi.org/10.1039/D5NR03806E.

[22] N.M.D. Brown, N. Cui, A. McKinley, An XPS study of the surface modification of natural MoS_2 following treatment in an RF-oxygen plasma, Appl. Surf. Sci. 134 (1998) 11–21, https://doi.org/10.1016/S0169-4332(98)00252-9.

[23] H. Nan, Z. Wang, W. Wang, Z. Liang, Y. Lu, Q. Chen, D. He, P. Tan, F. Miao, X. Wang, J. Wang, Z. Ni, Strong photoluminescence enhancement of MoS_2 through defect engineering and oxygen bonding, ACS Nano 8 (2014) 5738–5745, https://doi.org/10.1021/nn500532f.

[24] C. Jung, H.I. Yang, W. Choi, Effect of ultraviolet-ozone treatment on MoS_2 monolayers: comparison of chemical-vapor-deposited polycrystalline thin films and mechanically exfoliated single crystal flakes, Nanoscale Res. Lett. 14 (2019) 278, https://doi.org/10.1186/s11671-019-3119-3.

[25] A. Castellanos-Gomez, M. Barkelid, A.M. Goossens, V.E. Calado, H.S.J. van der Zant, G.A. Steele, Laser-thinning of MoS_2: on-demand generation of a single-layer semiconductor, Nano Lett. 12 (2012) 3187–3192, https://doi.org/10.1021/nl301164v.

[26] Y. Liu, H. Nan, X. Wu, W. Pan, W. Wang, J. Bai, W. Zhao, L. Sun, X. Wang, Z. Ni, Layer-by-layer thinning of MoS_2 by plasma, ACS Nano 7 (2013) 4202–4209, https://doi.org/10.1021/nn400644t.

[27] T. Lin, B. Kang, M. Jeon, C. Huffman, J. Jeon, S. Lee, W. Han, J. Lee, S. Lee, G. Yeom, K. Kim, Controlled layer-by-layer etching of MoS_2, ACS Appl. Mater. Interfaces 7 (2015) 15892–15897, https://doi.org/10.1021/acsami.5b03491.

[28] K.S. Kim, D. Lee, C.S. Chang, S. Seo, Y. Hu, S. Cha, H. Kim, J. Shin, J.H. Lee, S. Lee, J.S. Kim, K.H. Kim, J.M. Suh, Y. Meng, B.I. Park, J.H. Lee, H.S. Park, H.S. Kum, M. H. Jo, G.Y. Yeom, K. Cho, J.H. Park, S.H. Bae, J. Kim, Non-epitaxial single-crystal 2D material growth by geometric confinement, Nature 614 (2023) 88–94, https://doi.org/10.1038/s41586-022-05524-0.

[29] W. Chen, J. Zhao, J. Zhang, L. Gu, Z. Yang, X. Li, H. Yu, X. Zhu, R. Yang, D. Shi, X. Lin, J. Guo, X. Bai, G. Zhang, Oxygen-assisted chemical vapor deposition growth of large single-crystal and high-quality monolayer MoS_2, J. Am. Chem. Soc. 137 (2015) 15632–15635, https://doi.org/10.1021/jacs.5b10519.

[30] K.S. Kim, Y.J. Ji, K.H. Kim, S. Choi, D.H. Kang, K. Heo, S. Cho, S. Yim, S. Lee, J.-H. Park, Y.S. Jung, G.Y. Yeom, Ultrasensitive MoS_2 photodetector by serial nano-bridge multi-heterojunction, Nat. Commun. 10 (2019) 4701, https://doi.org/10.1038/s41467-019-12592-w.

[31] A. Splendiani, L. Sun, Y. Zhang, T. Li, J. Kim, C.Y. Chim, G. Galli, F. Wang, Emerging photoluminescence in monolayer MoS_2, Nano Lett. 10 (2010) 1271–1275, https://doi.org/10.1021/nl903868w.

[32] F. Xi, H. Sharma, X. Wu, T. Schram, D. Cott, R.K. Grubbs, P. Kumar, T.D. Ngo, S. Ghosh, F. Han, D. Van Dorp, D. Verreck, S. Sutar, Q. Smets, D. Lin, K. Banerjee, C.J. Lockhart De La Rosa, L. Goux, G.S. Kar, Integration of GAA monolayer MoS_2 nanosheet FETs with gate first process for future 2D CFET scaling, Eur. Solid-State Circuits Conf. (2024) 121–124, https://doi.org/10.1109/ESSERC62670.2024.10719449.